

# RS-OOD: A Vision-Language Augmented Framework for Out-of-Distribution Detection in Remote Sensing

Yingrui Ji<sup>1,2</sup>, Jiansheng Chen<sup>1,\*</sup>, Jingbo Chen<sup>1</sup> *Member, IEEE*, Anzhi Yue<sup>1</sup>, Chenhao Wang<sup>1,2</sup>, Kai Li<sup>1,2</sup>, Yao Zhu<sup>3</sup>

**Abstract**—Out-of-distribution (OOD) detection represents a critical challenge in remote sensing applications, where reliable identification of novel or anomalous patterns is essential for autonomous monitoring, disaster response, and environmental assessment. Despite remarkable progress in OOD detection for natural images, existing methods and benchmarks remain poorly suited to remote sensing imagery due to data scarcity, complex multi-scale scene structures, and pronounced distribution shifts. To this end, we propose RS-OOD, a novel framework that leverages remote sensing-specific vision-language modeling to enable robust few-shot OOD detection. Our approach introduces three key innovations: spatial feature enhancement that improved scene discrimination, a dual-prompt alignment mechanism that cross-verifies scene context against fine-grained semantics for spatial-semantic consistency, and a confidence-guided self-training loop that dynamically mines pseudo-labels to expand training data without manual annotation. RS-OOD consistently outperforms existing methods across multiple remote sensing benchmarks and enables efficient adaptation with minimal labeled data, demonstrating the critical value of spatial-semantic integration.

**Index Terms**—Out-of-distribution, Vision-Language Model, Remote Sensing.

## I. INTRODUCTION

REMOTE sensing models excel at classifying known remote sensing scenes, including land-cover types, artificial structures, and various geospatial objects. However, these models predominantly rely on the closed-world assumption during training, leading to a critical vulnerability when deployed in open-world environments: encountering out-of-distribution (OOD) inputs. In operational scenarios, remote sensing systems inevitably face novel objects and scene patterns not present in training datasets. Traditional approaches typically misclassify these unfamiliar inputs into the nearest known categories with unjustified high confidence. This overconfidence towards unknown factors undermines the reliability of automated geospatial analysis and poses severe safety risks. For instance, misidentifying newly emerged structures or disaster-affected regions can result in erroneous decisions in critical applications, potentially exacerbating the severity of emergency responses or urban planning strategies.

Despite the fundamental importance of robust scene understanding, specialized research addressing OOD detection in remote sensing remains limited. Existing OOD detection methods in computer vision have largely been developed under

well-supervised, data-rich conditions, a setting drastically different from the typical data scarcity scenarios encountered in remote sensing. Acquiring extensive labeled images covering every category or geographical region is hard; hence, models must generalize from a limited number of annotated examples. Moreover, remote sensing scenes inherently possess high complexity, where individual images frequently include objects spanning multiple scales and diverse semantic categories, embedded within vastly varying environmental backgrounds. This intrinsic complexity, combined with the distributional shifts caused by variations in sensors, geographical locations, or capture conditions, considerably intensifies the OOD detection challenge. Models trained within one geographical or sensor context often struggle to recognize novel patterns emerging in distinct regional settings, especially when such patterns appear within unfamiliar combinations or environmental contexts. These challenges underscore a significant gap in the current capabilities of remote sensing OOD detection.

The emergence of Vision-Language Models (VLMs) has opened new possibilities for OOD detection by enabling models to understand both visual patterns and semantic descriptions. These models have shown success in natural image domains by leveraging rich semantic information to identify distribution shifts. Recent developments in remote sensing have produced specialized VLMs, such as RemoteCLIP [1], designed to handle the unique characteristics of geospatial imagery. These models demonstrate improved understanding of remote sensing contexts compared to general-purpose VLMs. However, the lack of spatial awareness and the challenges posed by data scarcity limit the application of current vision-language model (VLM) based methods in the remote sensing applications.

To this end, we present RS-OOD, a novel framework specifically designed for few-shot OOD detection in remote sensing imagery, featuring three key innovations: spatial feature enhancement that focuses on important image regions; a dual-prompt alignment mechanism that cross-verifies scene context with fine-grained semantics to ensure spatial-semantic consistency; and a confidence-guided self-training loop that dynamically mines pseudo-labels to expand training data without manual annotation.

To enhance multimodal representation, RS-OOD employs spatial feature enhancement addresses the characteristics of remote sensing imagery through architecture-aware processing. The module employs parallel feature extraction at multiple scales to capture diverse spatial patterns, from local details to global context. An adaptive attention mechanism then focuses on critical regions to identify the discriminative features for

<sup>1</sup> Aerospace Information Research Institute, Chinese Academy of Sciences, Beijing, 100101, China.

<sup>2</sup> School of Electronic, Electrical and Communication Engineering, University of Chinese Academy of Sciences, Beijing, 100049, China.

<sup>3</sup> Zhejiang University, Hangzhou, 310058, China.

\* Corresponding author: Jiansheng Chen

OOD detection.

To further elevate the model’s spatial-semantic reasoning, we introduce a dual-prompt alignment mechanism. In RS-OOD, one set of prompts (global prompts) encodes whole scene context, while another (category-specific prompts) captures fine-grained, class-relevant details. By aligning visual features with both sets of prompts, RS-OOD conducts a robust spatial-semantic consistency check: only regions that align with both general context and specific category semantics are considered in-distribution, while those failing both tests are flagged as OOD.

To further exploit available data and enhance model robustness, we embed a confidence-guided self-training mechanism. By dynamically mining high-confidence pseudo-labels from unlabeled or weakly labeled samples, RS-OOD is able to automatically augment its training data. This self-training loop enables the model to iteratively refine its decision boundaries without requiring additional manual annotation, thus increasing the training data and enhancing model performance against both in-distribution errors and OOD confusion, especially in data-limited settings.

In summary, RS-OOD unifies spatially vision-language modeling, dual-prompt semantic alignment, and confidence-driven self-training within a single cohesive framework.

We comprehensively evaluate RS-OOD on 5 remote sensing benchmarks explicitly configured for OOD detection. These benchmarks include standard scene classification datasets (UCMerced\_LandUse [2], NWPU-RESISC45 [3], AID [4], EuroSAT\_RGB [5], WHU-RS19 [6]) under and cross-dataset scenarios, simulating real-world distributional shifts. Our method consistently achieves a high level of performance, significantly surpassing existing approaches under both normal and few-shot training conditions. For instance, on the UCMerced\_LandUse benchmarks, RS-OOD achieves consistently higher AUROC and AUPR scores — with maximum improvements of 23.13% and 21.66% observed in certain settings — even when trained with only a limited number of labeled examples per category. The RS-OOD framework exhibits not only robust detection capabilities for unseen categories but also generalization across different geographical regions and sensor domains.

In summary, our contributions are as follows:

- 1) We propose RS-OOD, a novel vision-language framework that enables effective few-shot out-of-distribution detection in remote sensing imagery.
- 2) We introduce a spatial feature enhancement module that captures multi-scale spatial relationships through attention mechanisms to improve scene discrimination in remote sensing imagery.
- 3) We introduce an innovative dual-prompt alignment mechanism to enhance the spatial semantic cross-verification between general scene context and fine-grained category-specific details.
- 4) We introduce a confidence-guided self-training mechanism that utilizes high-confidence pseudo-labels to effectively augment the training data and improve model robustness in few-shot scenarios without additional manual labeling.

## II. RELATED WORK

### A. OOD Detection in Remote Sensing

Deep learning models for remote sensing scene classification traditionally assume a closed-set paradigm, where all test samples belong to known classes seen during training. However, in real-world deployment, satellite and aerial imagery frequently contain novel land-cover types, unexpected objects, or anomalous Remote sensing models face a critical challenge when deployed in operational settings. While these models achieve high accuracy on test data from known categories, they often encounter unfamiliar objects or land-cover patterns in real-world imagery [7]. When this happens, models typically assign these unknown inputs to familiar categories with high confidence, leading to unreliable predictions [8], [9].

This problem stems from two fundamental characteristics of remote sensing data. First, obtaining labeled samples is expensive and time-consuming. Field validation requires ground surveys or expert interpretation, making it impractical to collect examples of every possible scene type [10]. Second, remote sensing scenes exhibit high complexity. A single image often contains objects at multiple scales—from individual buildings to entire agricultural fields—embedded within diverse backgrounds. This complexity makes it difficult to determine whether a region contains novel content or simply represents an unusual arrangement of known elements.

Recent studies have attempted to address OOD detection through various approaches. Classification-based methods modify traditional architectures to include an “unknown” category [11] or estimate uncertainty through probabilistic outputs [12], [13]. However, these require substantial changes to existing models and struggle with near-distribution anomalies. Reconstruction-based techniques use generative models to detect anomalies through reconstruction error [14], but suffer from high computational costs during inference. Feature-based approaches analyze internal representations of pre-trained models [15], [16]. These methods require extensive calibration data that may not be available in new geographical regions.

These methods, developed primarily for natural images, struggle with remote sensing’s unique challenges [17]. The combination of limited training data and complex spatial structures requires new approaches that can learn from a few examples while capturing the spatial relationships inherent in overhead imagery. Vision-language models offer a potential solution by leveraging semantic information to bridge the gap between limited visual examples and diverse operational scenarios.

### B. Vision-Language Models for Spatial-Semantic OOD Detection

Vision-language models like CLIP have changed how we approach OOD detection. By learning from millions of image-text pairs, CLIP can classify images using text descriptions alone [18]. This capability extends naturally to OOD detection—we can simply add an “unknown” category to the text labels [19], [20]. However, CLIP struggles with the specific requirements of remote sensing imagery [21].

The main issue is spatial awareness. CLIP generates a single feature vector for an entire image, which works well for natural photos but fails in remote sensing. Consider a satellite image of farmland with a small oil spill in one corner. CLIP might classify the entire image as "agricultural" while missing the localized anomaly. This problem has prompted several adaptation attempts. WinCLIP uses sliding windows to examine image patches separately [22], achieving good results on industrial defects [23]. Yet this approach requires processing each patch independently, increasing computation time significantly.

Another limitation is semantic verification. Current methods either focus on making ID classes more compact [24] or learning what "unknown" looks like [25], [26]. But remote sensing needs both perspectives. A residential area with unusual building patterns might match the general "urban" category while deviating from specific "residential" characteristics. Without checking both levels, the model produces false positives or misses subtle anomalies.

RemoteCLIP addresses the domain gap by pre-training on satellite imagery [1]. It understands overhead perspectives better than standard CLIP, improving zero-shot accuracy by 6.4% [27]. The CoOP framework suggests that learnable prompts could encode domain knowledge [28]. However, RemoteCLIP still lacks spatial reasoning. It processes entire scenes globally, missing the local details crucial for anomaly detection.

Recent work has tried various fixes. CLIPN learns a "no" prompt to reject OOD samples [26], [29]. CIBR reduces modality-specific noise through information bottlenecks [30]. These methods improve overall accuracy but require auxiliary OOD data during training—data that rarely exists in remote sensing applications.

### C. Few-Shot Learning and Self-Training Strategies

Remote sensing applications have sufficient labeled data, but few have accurate annotations. Collecting ground truth requires field surveys or expert annotation, limiting most datasets to tens or hundreds of samples per class [31]. This constraint has driven research into few-shot learning, where models must perform well with only 1-20 training examples per category. Prototypical networks have shown promise in this setting. Xi et al. developed networks that learn class prototypes from limited samples, achieving reasonable accuracy on hyperspectral datasets with just 10 examples per class [32]. Zhang et al. extended this by incorporating spatial relationships between objects, recognizing that certain land-cover types often appear together [33]. For instance, airports typically include runways, terminals, and parking areas in predictable arrangements. These spatial patterns help distinguish genuine scenes from anomalies even with few training samples. However, prototypical approaches assume that the few available samples represent the full class distribution. This assumption breaks down in remote sensing, where the same land-cover type varies significantly across regions [34]. Agricultural fields look different in Iowa versus India. Urban areas in Europe differ from those in Asia. Models trained on limited geographical samples fail when deployed elsewhere.

Self-training offers a solution by using unlabeled data to expand the training set. The key insight is that remote sensing has abundant unlabeled imagery—satellites continuously capture data worldwide. Bandara and Patel showed that consistency regularization could achieve near-supervised performance using only 10% labeled data [35]. Their method generates pseudo-labels for unlabeled samples, then trains on both real and pseudo-labeled data. The challenge lies in pseudo-label quality. Incorrect labels can reinforce errors and degrade performance. Fang et al. addressed this through confidence-based selection, only using predictions above a threshold [36]. Yuan and Lin took a different approach with temporal consistency—the same location should have similar labels across time unless changes occur [37]. Contrastive learning provides another angle. Mañas et al. introduced SeCo, which learns from seasonal variations without any labels [38]. Images of the same location in summer and winter share underlying structure despite appearance changes. This temporal consistency creates natural positive pairs for contrastive learning. Al-Hichri et al. combined this with few-shot learning, using contrastive pre-training to initialize models before fine-tuning on limited labeled data [39]. Despite these advances, existing methods have limitations for OOD detection. Prototypical networks focus on learning known classes, not identifying unknown ones [40]. Self-training methods typically assume all unlabeled data comes from known categories, but operational imagery contains novel patterns [41]. Confidence thresholds that work for classification may not transfer to OOD detection, where the model must distinguish "different but similar" from "genuinely unknown." The gap is evident. Few-shot OOD detection in remote sensing needs methods that can: learn from minimal examples of known classes, identify unknown patterns without OOD training data, and leverage unlabeled imagery while filtering out actual anomalies. Current approaches address pieces of this puzzle but lack integration. This motivates our framework combining spatial-aware few-shot learning with confidence-guided self-training specifically designed for OOD detection.

## III. METHOD

We propose RS-OOD, a framework for out-of-distribution detection in remote-sensing imagery. As shown in Fig. 1. First, we introduce spatial feature enhancement, which incorporates learnable textual prompts tied to specific image regions for spatial-aware feature extraction. Second, we propose a dual-prompt alignment mechanism that uses two sets of prompts to perform spatial-semantic consistency checks for OOD identification. Third, we devise a confidence-guided self-training strategy that iteratively refines the model using high-confidence predictions on unlabeled data, improving robustness in low-data regimes. We describe each component in detail below.

### A. Foundational Model

The RS-OOD framework is built upon RemoteCLIP, a vision-language model designed for remote sensing applications. RemoteCLIP differs from general-purpose models like

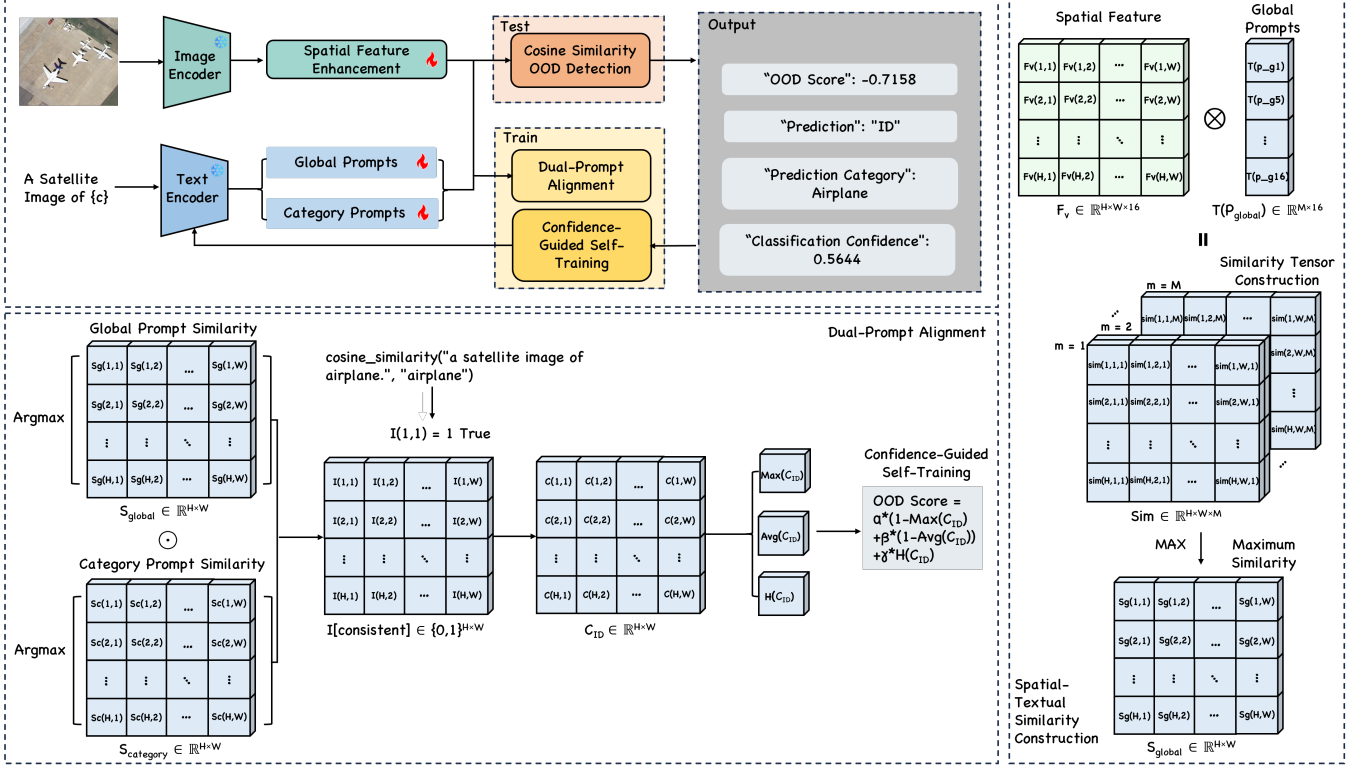


Fig. 1. The figure at the bottom shows the architecture of the RS-OOD framework. The system processes satellite images through an image encoder with spatial feature enhancement. A text encoder handles global prompts and category prompts. During testing, cosine similarity computation produces an OOD score (negative values indicate stronger ID tendency), enabling ID/OOD prediction and category classification. During training, dual-prompt alignment and confidence-guided self-training iteratively refine the model using high-confidence samples. The figure on the right shows the spatial-textual similarity construction. Category Prompt Similarity also has a similar process. The figure at the bottom shows the dual-prompt alignment mechanism.

CLIP by being pre-trained specifically on remote sensing image-text pairs. This domain-specific training enables the model to learn semantic representations aligned with overhead imagery characteristics. RemoteCLIP employs a dual-encoder architecture with an image encoder and a text encoder. The image encoder, typically a Vision Transformer (ViT), processes input image  $x_v$  and generates feature embedding  $f_v \in \mathbb{R}^D$ . The text encoder processes textual prompt  $x_t$  and produces text embedding  $f_t \in \mathbb{R}^D$ . During pre-training, the model aligns visual and textual representations through bidirectional contrastive learning. For a batch of  $N$  image-text pairs, the model calculates cosine similarities between all image-text combinations. The training objective maximizes similarity for matched pairs while minimizing it for mismatched pairs through symmetric contrastive loss:

$$\mathcal{L}_{\text{contrastive}} = \frac{1}{2} (\mathcal{L}_{i2t} + \mathcal{L}_{t2i}) \quad (1)$$

where the image-to-text loss is:

$$\mathcal{L}_{i2t} = -\frac{1}{N} \sum_{i=1}^N \log \frac{\exp(\text{sim}(f_{v,i}, f_{t,i})/\tau)}{\sum_{j=1}^N \exp(\text{sim}(f_{v,i}, f_{t,j})/\tau)} \quad (2)$$

and the text-to-image loss is:

$$\mathcal{L}_{t2i} = -\frac{1}{N} \sum_{i=1}^N \log \frac{\exp(\text{sim}(f_{t,i}, f_{v,i})/\tau)}{\sum_{j=1}^N \exp(\text{sim}(f_{t,i}, f_{v,j})/\tau)} \quad (3)$$

Here,  $\text{sim}(a,b)$  denotes cosine similarity  $\frac{a \cdot b}{\|a\| \|b\|}$ ,  $\tau$  is a learnable temperature parameter. For each positive pair  $(f_{v,i}, f_{t,i})$ , all other embeddings serve as hard negatives within the batch. This training process provides RemoteCLIP with zero-shot classification capability. The model classifies images by computing cosine similarity between image embeddings and text embeddings of class names.

## B. Spatial Feature Enhancement

Standard vision-language models generate single global feature vectors for entire images, which limits their effectiveness for remote sensing applications. Remote sensing scenes contain diverse objects and structures, including aircraft, buildings, infrastructure, and various land cover types. Out-of-distribution patterns may appear in localized spatial regions within these complex scenes. To address this limitation, RS-OOD incorporates spatial feature enhancement for improved scene discrimination.

The foundation of our approach leverages the patch-based architecture of vision transformers within RemoteCLIP. The image encoder processes an input image  $x_v$  and outputs a spatial feature map  $F_v \in \mathbb{R}^{H \times W \times D}$ , where  $H$  and  $W$  represent the spatial dimensions of the patch grid, and  $D$  is the feature dimension. This preserves spatial topology while maintaining semantic representations at each location.

We employ a dual-branch attention mechanism combining channel and spatial attention for enhanced feature representation. The spatial attention weights are computed as:

$$S_{\text{spatial}}(i, j) = \sigma \left( \text{Conv7} \times 7 \left( \text{Concat}(\text{Mean}_c(F_v), \text{Max}_c(F_v)) \right) \right)_{(i, j)} \quad (4)$$

where  $F_v^{ch} = F_v \odot \text{ChannelAtt}(F_v)$  represents the channel-attended features,  $\text{Max}_c(\cdot)$  denote channel-wise average and max pooling operations, and  $\sigma$  is the sigmoid activation function. This follows the Convolutional Block Attention Module architecture without any text encoder involvement.

To capture spatial relationships across scales, we incorporate neighborhood information. For each location  $(i, j)$ , we define a spatial context window  $\mathcal{N}_r(i, j)$  of radius  $r$  and compute an aggregated spatial score:

$$S_{\text{context}}(i, j) = \frac{1}{|\mathcal{N}_r(i, j)|} \sum_{(i', j') \in \mathcal{N}_r(i, j)} S_{\text{map}}(i', j') \cdot w(i - i', j - j') \quad (5)$$

The spatial weighting function emphasizes central locations:

$$w(\Delta i, \Delta j) = \exp \left( -\frac{(\Delta i)^2 + (\Delta j)^2}{2\sigma^2} \right) \quad (6)$$

where  $\sigma = r/3$  controls spatial decay rate. This Gaussian weighting ensures pixels closer to the center location  $(i, j)$  contribute more significantly while incorporating broader spatial neighborhood information.

The number of spatial prompts  $k$  balances representational capacity with computational efficiency:

$$k = \min \left( \lceil \log_2(D) \rceil \times 2, \frac{HW}{16} \right) \quad (7)$$

For typical applications with  $D = 512$  and resolution  $H \times W = 14 \times 14$ , this yields  $k \in [12, 16]$ . The radius  $r$  is determined based on the vision transformer's receptive field:

$$r = \max \left( 1, \left\lfloor \frac{\text{patch\_size}}{2} \right\rfloor \right) \quad (8)$$

For standard ViT configurations with  $16 \times 16$  patches, this results in  $r = 3$ , creating a  $7 \times 7$  neighborhood that captures local spatial dependencies with manageable computational overhead.

### C. Dual-Prompt Alignment Mechanism

To enhance detection reliability in the heterogeneous landscapes characteristic of remote sensing, we introduce a dual-prompt alignment mechanism that performs spatial-semantic consistency verification. This approach employs two distinct sets of learnable text prompts to model complementary aspects of the in-distribution data:

Global Prompts:  $\mathcal{P}_{\text{global}} = \{p_g^1, p_g^2, \dots, p_g^M\} \in \mathbb{R}^{M \times D}$ . encode holistic distributional patterns of ID scenes. These prompts are initialized from ID feature statistics:  $p_g^i = \mu_{\text{ID}} + \epsilon_i$ , where  $\mu_{\text{ID}} = \frac{1}{N_{\text{ID}}} \sum_{j=1}^{N_{\text{ID}}} f_v(x_j)$ , with  $\epsilon_i \sim \mathcal{N}(0, \sigma^2 I)$  providing controlled variation.

Category-Specific Prompts:  $\mathcal{P}_{\text{cat}} = \{p_c^1, p_c^2, \dots, p_c^C\} \in \mathbb{R}^{C \times D}$  capture fine-grained semantic details for each category.

These are initialized from class-wise centroids:  $p_c^k = \mu_k + \delta_k$ , where  $\mu_k = \frac{1}{|\mathcal{Y}_k|} \sum_{x_j \in \mathcal{Y}_k} f_v(x_j)$ , where  $\mathcal{Y}_k$  denotes the set of samples belonging to class  $k$ . For input image with a spatial feature map  $F_v \in \mathbb{R}^{H \times W \times D}$ , visual features at each location  $(i, j)$  are aligned with both prompt sets through normalized cosine similarity:

$$S_{\text{global}}(i, j) = \max_{m=1}^M \frac{F_v(i, j) \cdot \mathcal{T}(p_g^m)}{|F_v(i, j)| |\mathcal{T}(p_g^m)|} \quad (9)$$

$$S_{\text{cat}}(i, j) = \max_{k=1}^C \frac{F_v(i, j) \cdot \mathcal{T}(p_c^k)}{|F_v(i, j)| |\mathcal{T}(p_c^k)|} \quad (10)$$

where  $\mathcal{T}(\cdot)$  denotes the text encoder. A region is considered in-distribution when its features align with both global distribution patterns and specific category semantics.

The dual-verification process uses an ID-consistency score:

$$C_{\text{ID}}(i, j) = S_{\text{global}}(i, j) \cdot S_{\text{cat}}(i, j) \cdot \mathbb{I}[\text{consist}(g^*(i, j), c^*(i, j))] \quad (11)$$

where  $g^*(i, j) = S_{\text{global}}(i, j)$  and  $c^*(i, j) = S_{\text{cat}}(i, j)$  represent the activated global and category prompts at location  $(i, j)$ , and  $\mathbb{I}[\cdot]$  verifies semantic consistency between these activated prompts.

The framework computes OOD scores by measuring deviations from ID consistency patterns across spatial scales. The final OOD score combines three complementary measures:

$$\text{OOD Score} = \alpha(1 - C_{\text{max}}) + \beta(1 - C_{\text{avg}}) + \gamma \mathcal{H}(C_{\text{ID}}) \quad (12)$$

where  $\alpha, \beta, \gamma$  are learnable weights and  $\mathcal{H}(\cdot)$  measures spatial entropy of consistency scores across the feature map. The ID consistency score  $C_{\text{ID}}(i, j)$  combines both prompt alignments through element-wise multiplication, ensuring that regions must satisfy both global and category-specific criteria to be considered in-distribution.

The dual-prompt system is optimized through a composite objective that balances ID classification accuracy and prompt specialization:

$$L = \lambda_{\text{global}} L_{\text{global}} + \lambda_{\text{cat}} L_{\text{cat}} + \lambda_{\text{div}} \quad (13)$$

where  $L_{\text{global}}$  optimizes global prompts to capture overall ID distribution characteristics:

$$L_{\text{global}} = \text{CE}(\tau \cdot f_v P_{\text{global}}^\top, y_{\text{global}}) \quad (14)$$

with  $\tau$  as the temperature parameter and  $y_{\text{global}}$  representing binary ID/OOD labels.

$L_{\text{cat}}$  trains category-specific prompts for fine-grained classification within ID samples:

$$L_{\text{cat}} = \text{CE}(\tau \cdot f_v P_{\text{cat}}^\top, y_{\text{cat}}) \quad (15)$$

where  $y_{\text{cat}}$  denotes specific category labels for ID samples.

$L_{\text{div}}$  maintains diversity between global and category-specific prompts to prevent redundant representations:

$$L_{\text{div}} = -\frac{1}{MC} \sum_{i=1}^M \sum_{j=1}^C \cos(p_i^{\text{global}}, p_j^{\text{cat}}) \quad (16)$$

where  $M$  and  $C$  represent the numbers of global and category-specific prompts, respectively. The hyperparameters  $\lambda_{\text{global}}$ ,  $\lambda_{\text{cat}}$ , and  $\lambda_{\text{div}}$  controls the relative importance of each objective component.

#### D. Few-shot Training for OOD Detection

RS-OOD addresses the data scarcity challenge in remote sensing through few-shot OOD detection. Limited labeled data availability in geographical regions requires models to generalize from minimal annotated examples. We consider a K-shot, C-class problem with labeled training set  $\mathcal{D}_{\text{train}} = \{(x_i, y_i)\}_{i=1}^{N_L}$ , where  $N_L = K \times C$ .

The framework initializes prompts using statistics from available ID samples:

$$\mathbf{p}_g^{(0)} = \frac{1}{N_L} \sum_{i=1}^{N_L} f_v(x_i) + \epsilon, \quad \epsilon \sim \mathcal{N}(0, \sigma^2 \mathbf{I}) \quad (17)$$

where  $f_v(x_i)$  denotes visual features from the frozen VLM encoder. This initialization ensures prompts begin with ID-relevant information rather than random values.

Category-specific prompts employ prototype-based initialization:

$$\mathbf{p}_c^{(0)} = \frac{1}{K} \sum_{x_j \in \mathcal{Y}_c} f_v(x_j) + \delta_c, \quad c = 1, \dots, C \quad (18)$$

where  $\mathcal{Y}_c$  represents the K samples of class C. Each category prompt captures class-specific patterns from minimal examples.

The expected OOD detection performance can be bounded as:

$$\mathbb{P}(\text{correct detection}) \geq 1 - \exp\left(-\frac{K \cdot d_{\min}^2}{2\sigma^2}\right) \quad (19)$$

where  $d_{\min}$  is the minimum distance between ID and OOD clusters, and  $\sigma^2$  is the within-class variance. This bound shows that reliable detection is achievable with a small K when the feature space provides good separation.

The approach optimizes only task-specific prompts (typically  $M+C$  vectors, where  $M \ll C$ ), adapting the foundation model without overfitting. This parameter-efficient design suits remote sensing applications where new regions or sensor modalities provide limited labeled data.

#### E. Confidence-Guided Self-Training

To reinforce model robustness in few-shot settings, RS-OOD integrates a confidence-guided self-training mechanism. This component utilizes abundant unlabeled remote sensing imagery to expand the training set without manual supervision. The dual-prompt alignment mechanism provides confidence estimation for both ID classification and OOD detection. Unlike conventional methods that rely solely on classification confidence, our framework uses spatial-semantic consistency between global and category-specific prompts to identify reliable pseudo-labels while filtering potential OOD samples. For model  $f_\theta$  trained on  $\mathcal{D}_{\text{train}}$ , we identify high-confidence unlabeled samples where prediction uncertainty is bounded:

$$\mathcal{H}(f_\theta(x)) = - \sum_{c=1}^C p(c|x) \log p(c|x) < \epsilon \quad (20)$$

After initial training, the model generates predictions on the unlabeled pool  $\mathcal{D}_U$ . For each sample, we compute predicted class and confidence:

$$\hat{y} = \arg \max_c p(c|x), \quad \text{conf}(x) = \max_c p(c|x) \quad (21)$$

The adaptive threshold considers data distribution and task complexity:

$$\lambda = \mu_{\text{conf}} - \alpha \cdot \sigma_{\text{conf}} \quad (22)$$

where  $\mu_{\text{conf}}$  and  $\sigma_{\text{conf}}$  are the mean and standard deviation of confidence scores on correctly classified training samples.

The pseudo-labeled dataset is constructed through:

$$\mathcal{D}_P = \{(x, \hat{y}) \mid x \in \mathcal{D}_U, \text{conf}(x) > \lambda, \text{cons}(x) > \tau\} \quad (23)$$

where prediction consistency across augmented views is measured as:

$$\text{cons}(x) = \frac{1}{|\mathcal{A}|} \sum_{a \in \mathcal{A}} \mathbb{I}[\hat{y}_a = \hat{y}] \quad (24)$$

The augmented training set  $\mathcal{D}'_{\text{train}} = \mathcal{D}_{\text{train}} \cup \mathcal{D}_P$  refines the model through weighted loss:

$$\mathcal{L}_{\text{total}} = \mathcal{L}_{\text{ID}}(\mathcal{D}_{\text{train}}) + \beta \cdot \mathcal{L}_{\text{ID}}(\mathcal{D}_P) + \gamma \cdot \mathcal{L}_{\text{reg}} \quad (25)$$

where  $\beta < 1$  down-weights pseudo-labeled samples to account for potential label noise.

To prevent distribution drift, we monitor feature distributions using Gaussian Mixture Models:

$$p(f_v|\mathcal{D}) = \sum_{i=1}^K \pi_i \mathcal{N}(f_v; \mu_i, \Sigma_i) \quad (26)$$

The KL divergence between training and pseudo-labeled distributions is computed as:

$$\text{KL}_{\text{drift}} = \int p(f_v|\mathcal{D}_{\text{train}}) \log \frac{p(f_v|\mathcal{D}_{\text{train}})}{p(f_v|\mathcal{D}_P)} df_v \quad (27)$$

The drift threshold is set based on natural variance within training distribution:

$$\theta_{\text{drift}} = \mu_{\text{intra}} + 2\sigma_{\text{intra}} \quad (28)$$

If  $\text{KL}_{\text{drift}} > \theta_{\text{drift}}$ , self-training stops to prevent model degradation. This mechanism ensures stable performance improvement while maintaining the original ID distribution characteristics.

## IV. EXPERIMENTS

### A. Datasets

UCMerced\_LandUse [2] is a widely-used remote sensing scene classification dataset containing 2,100 aerial images. The dataset comprises 21 land-use categories with 100 images per class, each measuring 256×256 pixels with a spatial resolution of 0.3 meters. Images were manually extracted from the USGS National Map Urban Area Imagery collection, covering various urban areas across the United States. Categories include agricultural, airplane, baseball diamond, beach, buildings, and forest, among others.

NWPU-RESISC45 [3] represents one of the largest publicly available remote sensing scene classification benchmarks. It

contains 31,500 images distributed across 45 scene classes, with 700 images per category. Each image has a size of 256×256 pixels and covers diverse spatial resolutions ranging from 0.2 to 30 meters. The dataset was created by Northwestern Polytechnical University using Google Earth imagery and encompasses a wide variety of scene types including airports, bridges, churches, and industrial areas.

AID (Aerial Image Dataset) [4] consists of 10,000 aerial images organized into 30 scene categories. The dataset features images of 600×600 pixels collected from Google Earth with varying spatial resolutions between 0.5 and 8 meters. Each class contains between 220 to 420 samples, covering diverse geographic regions primarily in China. Scene categories include both natural landscapes (desert, forest, mountain) and man-made structures (airport, bridge, commercial area).

EuroSAT\_RGB [5] is derived from Sentinel-2 satellite imagery, comprising 27,000 labeled patches across 10 land use and land cover classes. Each image patch measures 64×64 pixels with a consistent spatial resolution of 10 meters. The dataset covers urban and rural areas across 34 European countries, with 2,000-3,000 samples per class. Categories include residential areas, highways, industrial buildings, permanent crops, and pastures.

WHU-RS19 [6] is a high-resolution satellite image dataset containing 1,005 images distributed among 19 scene classes. Images were collected from Google Earth with a spatial resolution of up to 0.5 meters and a size of 600×600 pixels. The dataset includes approximately 50 images per category, covering various scene types such as airports, beaches, bridges, commercial areas, and residential areas. It serves as a benchmark for evaluating scene classification algorithms in high-resolution remote sensing applications.

## B. Experimental Setup

Our experiments leverage RemoteCLIP/ViT-B/32 as the foundational model, which is specifically designed for remote sensing imagery. We freezed all parameters of the visual encoder and text encoder, and only introduces a learnable spatial cue vector and a dual cue alignment mechanism (including category-specific ID cues and general OOD cues) to achieve spatially aware fine-grained OOD detection without changing the weights of the original model, and further improves the detection performance in few-shot scenarios through confidence-guided self-training.

For the few-shot learning experiments, we construct limited training subsets from the complete datasets. Specifically, we select 15 categories(Airplane, BareLand, Beach, Bridge, Building, Desert, Farmland, Freeway, Green\_LandCover, Harbor, Intersection, Meadow, Mountain, Parking, Sports\_Facility) as ID classes, with each category containing 100 images. In the K-shot learning scenario, K samples are randomly sampled from each ID category to form the training set. This study primarily adopts a 4-shot setting, using only 4 training samples per category, resulting in a total of 60 labeled samples for model training. Regarding prompt learning configuration, ID prompts are designed with one-to-one correspondence to specific categories, where each

category is assigned a learnable prompt vector while retaining the original category name information to maintain semantic associations. In contrast, OOD prompts consist of 16 generic learnable vectors without specific category semantics.

Training employs the AdamW optimizer. And we set the hyperparameters: 3 training epochs, learning rate of 0.0001, and batch size of 32. To comprehensively evaluate RS-OOD’s performance, we compare it against seven established OOD detection baselines: MSP (Maximum Softmax Probability) [42], Energy-based [43] detection, MaxLogit [44], Entropy [45], ODIN [46], and GradNorm [47]. All methods utilize the same RemoteCLIP/ViT-B/32 pre-trained model as the feature extractor to ensure fair comparison. We adopt three widely-used evaluation metrics: FPR95 (False Positive Rate at 95% True Positive Rate), which measures the false positive rate when maintaining high recall; AUROC (Area Under the Receiver Operating Characteristic curve), which provides a comprehensive assessment across different thresholds; and AUPR (Area Under the Precision-Recall curve), which is particularly sensitive to performance on imbalanced datasets where OOD samples are relatively rare.

## C. Evaluation method

Fig. 2 illustrates the score distributions of ID and OOD samples before and after applying the RS-OOD framework across three remote sensing datasets. For the EuroSAT\_RGB dataset shown in subfigures (a) and (b), the baseline RemoteCLIP results exhibit substantial overlap between ID and OOD distributions. The ID samples (blue) show a broad distribution centered around 0.6-0.8, while OOD samples (green) concentrate near 1.0, leading to classification ambiguity. After applying RS-OOD, the ID distribution shifts toward lower scores (0.0-0.2), while the OOD distribution remains concentrated near 1.0 with reduced variance. The NWPU-RESISC45 dataset results in subfigures (c) and (d) demonstrate even more significant improvements. The baseline RemoteCLIP shows extensive distribution overlap, with ID samples spreading across a wide range from 0.2 to 1.0. After applying RS-OOD, a clear bimodal separation emerges, with ID samples concentrating in the lower score region (0.0-0.4) while OOD samples maintain their high-score characteristics. This dataset achieves the most pronounced improvement among the three evaluated datasets, with virtually no overlap between distributions. For the AID dataset shown in subfigures (e) and (f), the baseline RemoteCLIP exhibits a similar overlapping pattern, with ID samples clustering around 0.6-0.8 and OOD samples peaking near 1.0. The RS-OOD framework successfully addresses this issue by pushing the ID distribution toward lower scores (0.0-0.3) while maintaining OOD concentration at high values. The separation achieved on AID is comparable to EuroSAT\_RGB results.

**Feature Representation Visualization.** Based on the t-SNE visualization of WHU-RS19 dataset on Fig. 3, the feature representation demonstrates a meaningful clustering pattern where in-distribution (ID) and out-of-distribution (OOD) samples exhibit partial overlap across multiple semantic clusters. This distribution pattern aligns with the expected behavior

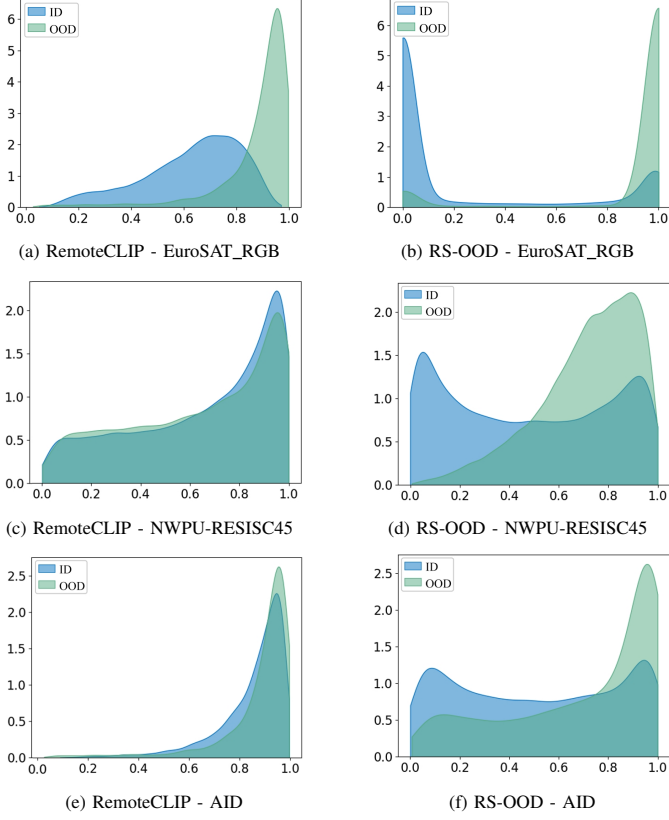


Fig. 2. Score distributions of ID and OOD samples across different datasets or settings. In each pair: RemoteCLIP baseline (left) and RS-OOD (right) result. RS-OOD consistently improves the separation between ID and OOD samples.

described in the RS-OOD framework, particularly considering the presence of overlapping categories between ID and OOD datasets. The mixed clustering observed in the visualization indicates that the model successfully learns semantic similarities rather than merely distinguishing dataset origins. This is evidenced by the formation of distinct clusters where semantically similar scenes from both ID and OOD distributions naturally group together, suggesting that the learned features capture genuine scene characteristics such as land cover types, spatial structures, and object compositions. Some clusters show predominantly ID samples while others contain balanced mixtures, indicating that certain scene types are more distinctive to the training distribution while others share common visual patterns across datasets. This behavior validates the effectiveness of the dual-prompt alignment mechanism, which performs spatial-semantic consistency checks rather than forcing artificial separation. The presence of mixed clusters is particularly important in remote sensing applications where similar land cover patterns may appear across different geographical regions or acquisition conditions, making strict ID-OOD separation both unrealistic and potentially detrimental to practical deployment.

**Few-shot Configuration Optimization.** Based on Fig. 4, RS-OOD demonstrates a consistent non-monotonic performance pattern across all five remote sensing datasets, with 4-shot configuration achieving optimal results. The average AUROC increases progressively from 62.98% (1-shot) to

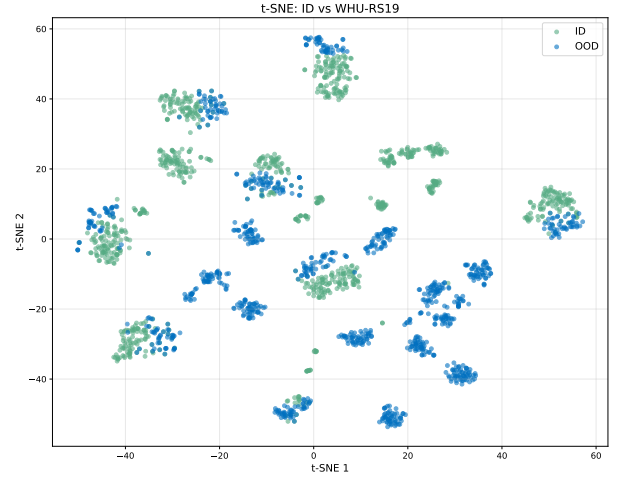


Fig. 3. Out-of-distribution detection performance on the WHU-RS19 dataset across different numbers of training shots. The 4-shot configuration achieves optimal performance across all metrics.

64.01% (4-shot), while average FPR95 decreases from 89.63% to 88.36%. Performance subsequently degrades at 8-shot (AUROC: 63.19%, FPR95: 89.06%), confirming the optimal training regime. Dataset-specific analysis reveals consistent 4-shot superiority despite varying scene characteristics. UCMerced LandUse achieves its best AUROC of 56.19% and lowest FPR95 of 88.24% at 4-shot, representing a balanced improvement for urban land-use categories. NWPU-RESISC45, with its 45 diverse scene classes, shows pronounced gains with AUROC reaching 65.50% and FPR95 dropping to 87.45%. AID dataset exhibits the strong performance, achieving 72.38% AUROC and 77.54% FPR95, reflecting the framework's effectiveness on high-resolution aerial imagery. EuroSAT RGB, despite its agricultural focus and spectral uniformity, maintains the optimization pattern with 63.19% AUROC at 4-shot. WHU-RS19 reaches peak AUROC of 69.96% and minimum FPR95 of 81.49%, demonstrating consistent behavior across high-resolution satellite scenes. The universal 4-shot optimum across datasets with different spatial resolutions, spectral characteristics, and scene complexities indicates that this configuration provides optimal balance between sample diversity and generalization capability. The performance degradation at 8-shot suggests that additional training samples from limited categories introduce overfitting effects that compromise OOD discrimination, regardless of dataset origin or scene type.

The optimal configuration identified above was subsequently used to evaluate RS-OOD against baseline methods. To better understand the practical implications of our framework before examining the comparative results, Fig. 5 illustrates representative detection examples from NWPU-RESISC45. The framework correctly identifies diverse ID scenes—including bridge, desert, intersection, and beach. It assigns low confidence scores to OOD samples such as sea ice, snowberg, terrace, and chaparral. This confidence separation is particularly notable given the visual similarities between certain ID and OOD pairs; for instance, snowberg's textural patterns resemble desert landscapes, yet the dual-prompt

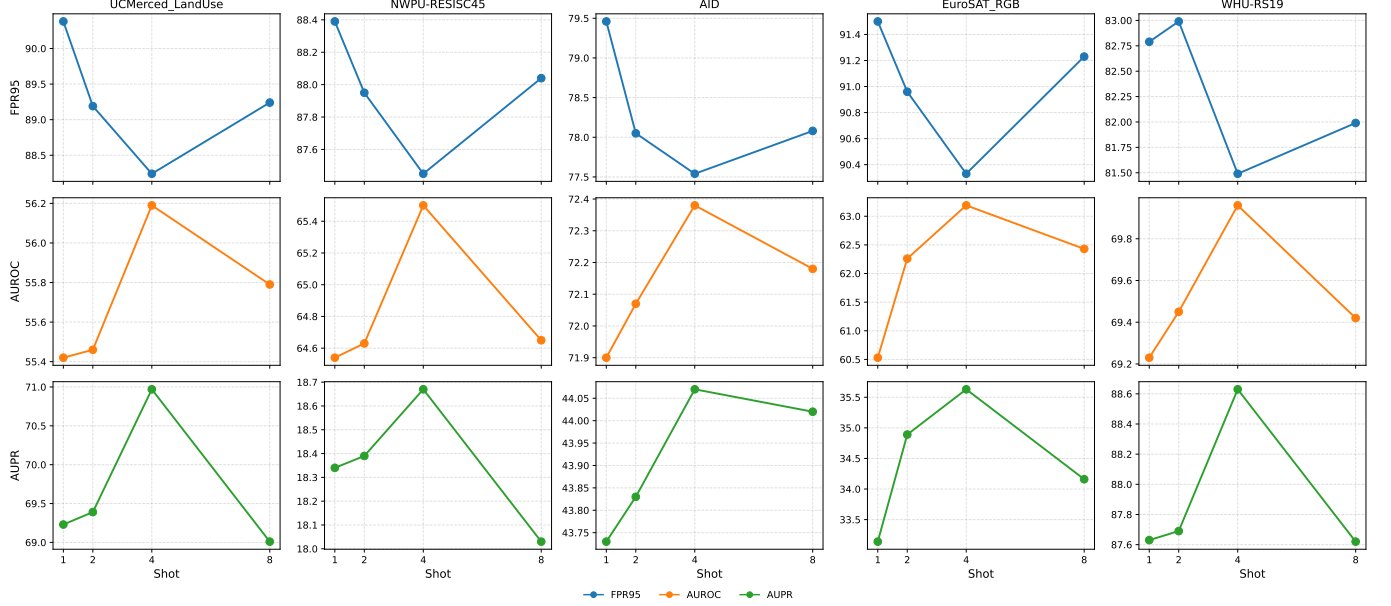


Fig. 4. Out-of-distribution detection performance on the 5 datasets across different numbers of training shots. The 4-shot configuration achieves optimal performance across all metrics.

alignment mechanism successfully detects subtle semantic deviations. These qualitative results demonstrate that RS-OOD’s performance improvements, as detailed in the following comparative analysis, stem from its ability to capture nuanced distributional differences even in visually ambiguous cases.

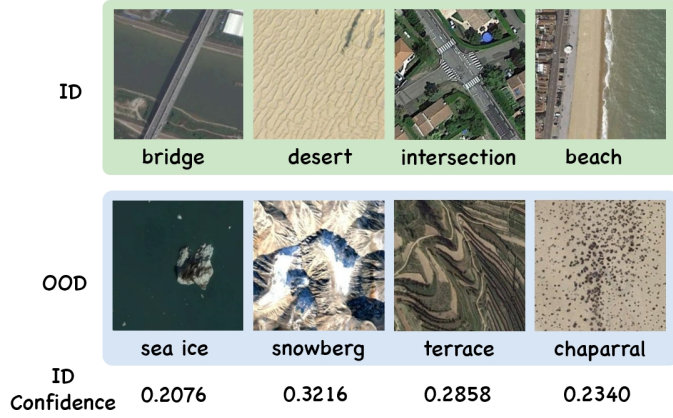


Fig. 5. Qualitative comparison of ID and OOD sample detection using RS-OOD. The top row shows correctly classified in-distribution samples from known categories, while the bottom row presents out-of-distribution samples with their corresponding ID confidence scores.

**Comparison with Baseline Methods.** The experimental results show the testing of basic OOD detection methods on remote sensing data. As shown in Table I. Traditional OOD detection methods exhibit fundamental limitations when applied to remote sensing imagery due to misaligned theoretical assumptions with domain characteristics.

The RS-OOD framework demonstrates method-specific enhancement patterns across diverse remote sensing datasets, with performance gains varying substantially based on the alignment between baseline method assumptions and dataset

characteristics. MSP achieves its most significant improvements on NWPU-RESISC45 (AUROC: 56.52% to 63.43%) and EuroSAT\_RGB (40.01% to 48.04%), where the dual-prompt alignment effectively addresses global confidence miscalibration. However, performance slightly degrades on UCMerced\_LandUse (AUROC: 42.53% to 41.55%), confirming that diverse urban textures resist simple confidence-based corrections. Energy-based detection shows consistent AUROC improvements across all datasets, with UCMerced\_LandUse exhibiting the largest gain (43.04% to 51.73%). The spatial feature enhancement particularly benefits datasets with complex urban scenes. The method achieves balanced improvements on NWPU-RESISC45 and AID, where spatial-semantic alignment helps differentiate fine-grained categories. MaxLogit demonstrates remarkable AUROC improvements on AID (43.50% to 52.91%) and EuroSAT\_RGB (52.87% to 64.60%), where spatial regularization effectively controls outlier activations. Performance marginally decreases on UCMerced\_LandUse (39.76% to 38.27%), validating concerns about artificial high-activation regions in uniform scenes. The framework consistently reduces FPR95 across all datasets, indicating improved threshold stability despite occasional AUROC fluctuations. ODIN shows modest improvements, with the best gains on EuroSAT\_RGB (AUROC: 48.15% to 54.20%) where temperature scaling benefits from spatial guidance. Performance remains relatively stable or slightly degrades on datasets with fine-grained urban categories (UCMerced, AID), confirming that pixel-level perturbations fail to enhance discrimination. WHU-RS19 exhibits minimal change (57.47% to 57.01%), suggesting incompatibility between uniform temperature scaling and diverse object scales. Entropy achieves substantial gains on AID (AUROC: 44.38% to 54.11%) and moderate improvements on most datasets, though NWPU-RESISC45 shows slight degradation (53.81%

TABLE I

THE TABLE SHOWS THE AUROC (HIGHER IS BETTER), AND AUPR (HIGHER IS BETTER) PERFORMANCE COMPARISON OF VARIOUS BASIC OOD METHODS AND THEIR COMBINATION WITH THE RS-OOD FRAMEWORK ON FIVE REMOTE SENSING DATASETS. METHOD\_RS-OOD IS THE RESULT OF COMBINING OUR METHOD.

Criterion	Method	UCMerced_LandUse		NWPU-RESISC45		AID		EuroSAT_RGB		WHU-RS19		Average	
		AUROC↑	AUPR↑	AUROC↑	AUPR↑	AUROC↑	AUPR↑	AUROC↑	AUPR↑	AUROC↑	AUPR↑	AUROC↑	AUPR↑
MSP	RemoteCLIP	42.53	62.29	56.52	<b>23.14</b>	62.83	34.46	40.01	<b>24.08</b>	58.63	76.39	51.90	44.07
	<b>RS-OOD</b>	<b>41.55</b>	<b>62.38</b>	<b>63.43</b>	19.51	<b>65.94</b>	<b>34.50</b>	<b>48.04</b>	21.76	<b>66.01</b>	<b>87.36</b>	<b>56.99</b>	<b>45.50</b>
Energy	RemoteCLIP	43.04	52.22	43.88	<b>9.92</b>	56.23	<b>36.59</b>	60.45	<b>37.98</b>	57.57	<b>80.90</b>	52.23	<b>43.52</b>
	<b>RS-OOD</b>	<b>51.73</b>	<b>61.83</b>	<b>52.58</b>	9.02	<b>60.71</b>	31.91	<b>69.77</b>	30.31	<b>63.38</b>	78.69	<b>59.63</b>	42.35
MaxLogit	RemoteCLIP	<b>39.76</b>	<b>58.74</b>	42.56	15.88	43.50	34.86	52.87	40.09	52.72	78.54	46.28	45.62
	<b>RS-OOD</b>	38.27	58.34	<b>47.97</b>	<b>16.22</b>	<b>52.91</b>	<b>35.15</b>	<b>64.60</b>	<b>43.74</b>	<b>55.05</b>	<b>81.65</b>	<b>51.76</b>	<b>47.02</b>
Odin	RemoteCLIP	28.64	46.29	43.57	<b>13.70</b>	44.12	<b>34.31</b>	48.15	21.57	<b>57.47</b>	<b>76.97</b>	44.39	<b>38.57</b>
	<b>RS-OOD</b>	<b>30.99</b>	<b>51.96</b>	<b>48.53</b>	10.19	<b>49.96</b>	28.56	<b>54.20</b>	<b>21.80</b>	57.01	76.80	<b>48.14</b>	37.86
Entropy	RemoteCLIP	49.03	56.43	<b>53.81</b>	23.67	44.38	<b>34.31</b>	57.85	43.49	56.39	76.78	52.29	46.94
	<b>RS-OOD</b>	<b>53.34</b>	<b>66.46</b>	51.99	<b>26.04</b>	<b>54.11</b>	34.01	<b>62.99</b>	<b>45.55</b>	<b>58.67</b>	<b>83.31</b>	<b>56.22</b>	<b>51.07</b>
GradNorm	RemoteCLIP	48.78	59.72	55.19	<b>19.84</b>	<b>54.18</b>	<b>39.91</b>	57.73	<b>27.96</b>	51.11	72.95	53.40	44.08
	<b>RS-OOD</b>	<b>58.61</b>	<b>69.83</b>	<b>68.11</b>	18.94	53.14	37.83	<b>57.92</b>	27.31	<b>59.39</b>	<b>82.34</b>	<b>59.43</b>	<b>47.25</b>

TABLE II

ABLATION STUDY OF BASELINE REMOTECLIP AND ENHANCEMENTS ACROSS 5 REMOTE SENSING BENCHMARKS. EACH ROW REPRESENTS A METHOD VARIANT: REMOTECLIP (RC), WITH OOD PROMPT OPTIMIZATION (+ OP), SPATIAL FEATURE ENHANCEMENT (+ SE), AND COMPLETE RS-OOD FRAMEWORK WITH SELF-TRAINING. COLUMNS REPORT DATASET-SPECIFIC RESULTS USING THREE COMPLEMENTARY METRICS. BOLD VALUES INDICATE BEST PERFORMANCE PER DATASET.

Method	UCMerced_LandUse		NWPU-RESISC45		AID		EuroSAT_RGB		WHU-RS19		Average	
	AUROC↑	AUPR↑	AUROC↑	AUPR↑	AUROC↑	AUPR↑	AUROC↑	AUPR↑	AUROC↑	AUPR↑	AUROC↑	AUPR↑
RemoteCLIP (RC)	47.28	64.86	59.39	17.87	62.01	37.71	39.66	13.97	63.94	86.28	54.45	44.14
RC + OOD-Prompt (OP)	50.96	66.97	64.53	20.42	67.19	41.30	50.80	24.42	67.37	87.36	60.17	48.10
RC + OP + Spatial Enhancement (SE)	51.85	67.28	64.22	18.46	67.41	41.45	55.35	27.09	67.48	87.06	61.15	48.04
<b>RC + OP + SE + Self-training (RS-OOD)</b>	<b>56.19</b>	<b>70.97</b>	<b>65.70</b>	<b>18.67</b>	<b>72.30</b>	<b>44.05</b>	<b>62.79</b>	<b>35.63</b>	<b>69.26</b>	<b>87.63</b>	<b>65.25</b>	<b>51.39</b>

to 51.99%) due to accumulated pseudo-labeling noise in multi-scale scenarios. The framework effectively reduces uncertainty in well-defined categories while maintaining reasonable performance on naturally ambiguous classes, as evidenced. GradNorm exhibits the most dramatic improvements, particularly on NWPU-RESISC45 (AUROC: 55.19% to 68.11%) and UCMerced\_LandUse (48.78% to 58.61%), where spatial prompts create stronger gradient signals. Performance slightly decreases on AID (54.18% to 53.14%), where fine-grained categories produce weak gradient variations that spatial decomposition further dilutes. The method maintains stable performance on EuroSAT\_RGB, with marginal AUROC improvement.

#### D. Ablation study

In this section, we perform an ablation study to systematically evaluate the contribution of each component within our proposed RS-OOD framework. The results are summarized in Table II. Ablation studies show that remote sensing OOD detection faces great challenges due to the high visual similarity between ID samples and OOD samples. The RS-OOD framework shows varying performance improvements across datasets on NWPU-RESISC45. This variation reflects different levels of ID/OOD overlap in each dataset. The OOD prompt optimization component contributes most notably to datasets containing OOD samples, where the AUROC improvement reaches 28.1% on AID dataset, indicating its ability to capture subtle semantic boundaries. The spatial enhancement mechanism exhibits dataset-specific effectiveness. On datasets with

simple spatial structures like EuroSAT\_RGB, the improvement remains minimal (0.11% AUROC increase), while complex urban scenes in AID benefit more substantially (4.55% improvement). This pattern suggests that spatial context information becomes valuable primarily in scenes with rich spatial variations and localized OOD targets. The self-training strategy further amplifies these improvements through a synergistic effect. On NWPU-RESISC45, the complete framework achieves a 10.29% FPR95 reduction in the final stage, exceeding the sum of previous improvements (6.92%), which indicates positive feedback loops in pseudo-label refinement.

#### V. CONCLUSION

In this paper, we propose RS-OOD, a few-shot out-of-distribution (OOD) detection framework for remote sensing imagery built upon the RemoteCLIP vision-language backbone. The framework's core innovations include spatial feature enhancement, a dual-prompt alignment mechanism, and a confidence-guided self-training loop, which respectively enhance location-aware semantic alignment, cross-verification between global and category-level semantics, and efficient exploitation of unlabeled data. Comprehensive experiments on five remote sensing benchmarks show that RS-OOD substantially improves AUROC and AUPR metrics under extremely limited labeled data. Overall, our study delivers an efficient and adaptable solution for OOD detection in remote sensing and establishes a strong foundation for future applications of multimodal modeling and self-supervised learning in Earth observation. We hope this work will inspire further research

leveraging spatial-semantic integration and few-shot learning to drive innovation and practical adoption of remote sensing OOD detection technologies.

## REFERENCES

- [1] F. Liu, D. Chen, Z. Guan, X. Zhou, J. Zhu, Q. Ye, L. Fu, and J. Zhou, “Remoteclip: A vision language foundation model for remote sensing,” *arXiv preprint arXiv:2306.11029*, 2023.
- [2] Y. Yang and S. Newsam, “Bag-of-visual-words and spatial extensions for land-use classification,” in *Proceedings of the 18th SIGSPATIAL international conference on advances in geographic information systems*, 2010, pp. 270–279.
- [3] G. Cheng, J. Han, and X. Lu, “Remote sensing image scene classification: Benchmark and state of the art,” *Proceedings of the IEEE*, vol. 105, no. 10, p. 1865–1883, Oct. 2017. [Online]. Available: <http://dx.doi.org/10.1109/JPROC.2017.2675998>
- [4] G.-S. Xia, J. Hu, F. Hu, B. Shi, X. Bai, Y. Zhong, L. Zhang, and X. Lu, “Aid: A benchmark data set for performance evaluation of aerial scene classification,” *IEEE Transactions on Geoscience and Remote Sensing*, vol. 55, no. 7, p. 3965–3981, Jul. 2017. [Online]. Available: <http://dx.doi.org/10.1109/TGRS.2017.2685945>
- [5] P. Helber, B. Bischke, A. Dengel, and D. Borth, “Eurosat: A novel dataset and deep learning benchmark for land use and land cover classification,” *IEEE Journal of Selected Topics in Applied Earth Observations and Remote Sensing*, 2019.
- [6] G.-S. Xia, W. Yang, J. Delon, Y. Gousseau, H. Sun, and H. Maître, “Structural high-resolution satellite image indexing,” 2009.
- [7] D. Tuia, C. Persello, and L. Bruzzone, “Toward a systematic review of domain adaptation for earth observation data,” *IEEE Geoscience and Remote Sensing Magazine*, vol. 9, no. 2, pp. 5–21, 2021.
- [8] D. Hendrycks and K. Gimpel, “A baseline for detecting misclassified and out-of-distribution examples in neural networks,” in *International Conference on Learning Representations*, 2017.
- [9] S. Liang, Y. Li, and R. Srikanth, “Enhancing the reliability of out-of-distribution image detection in neural networks,” in *International Conference on Learning Representations*, 2018.
- [10] J. Yang and et al., “A survey on open-set and open-world recognition,” *IEEE Transactions on Pattern Analysis and Machine Intelligence*, 2023.
- [11] W. Liu, X. Nie, B. Zhang, and X. Sun, “Incremental learning with open-set recognition for remote sensing image scene classification,” *IEEE Transactions on Geoscience and Remote Sensing*, vol. 60, pp. 1–16, 2022.
- [12] M. M. Al Rahhal, Y. Bazi, R. Al-Dayil, B. M. Alwadei, N. Ammour, and N. Alajlan, “Energy-based learning for open-set classification in remote sensing imagery,” *International Journal of Remote Sensing*, vol. 43, no. 18, pp. 6027–6037, 2022.
- [13] J. Gawlikowski, S. Saha, A. M. Kruspe, and X. X. Zhu, “An advanced dirichlet prior network for out-of-distribution detection in remote sensing,” *IEEE Transactions on Geoscience and Remote Sensing*, vol. 60, pp. 1–19, 2022.
- [14] G. Le Bellier, N. Audebert, and et al., “Detecting out-of-distribution earth observation images with diffusion models,” in *Proceedings of the IEEE/CVF Conference on Computer Vision and Pattern Recognition Workshops (EarthVision)*, 2024.
- [15] S. Li, N. Li, M. Jing, C. Ji, and L. Cheng, “Evaluation of ten deep-learning-based out-of-distribution detection methods for remote sensing image scene classification,” *Remote Sensing*, vol. 16, no. 9, p. 1501, 2024.
- [16] Y. Ji, Y. Zhu, Z. Li, J. Chen, Y. Kong, and J. Chen, “Enhancing out-of-distribution detection through dynamic activation function,” in *ICASSP 2025 - 2025 IEEE International Conference on Acoustics, Speech and Signal Processing (ICASSP)*, 2025, pp. 1–5.
- [17] B. Du and et al., “Out-of-distribution detection in remote sensing imagery,” *IEEE Journal of Selected Topics in Applied Earth Observations and Remote Sensing*, 2023.
- [18] A. Radford, J. W. Kim, C. Hallacy, A. Ramesh, G. Goh, S. Agarwal, G. Sastry, A. Askell, P. Mishkin, J. Clark, G. Krueger, and I. Sutskever, “Learning transferable visual models from natural language supervision,” in *Proceedings of the 38th International Conference on Machine Learning (ICML)*, vol. 139, 2021, pp. 8748–8763.
- [19] C. Jia, Y. Yang, Y. Xia, Y.-T. Chen, Z. Parekh, H. Pham, Q. Le, Y.-H. Sung, Z. Li, and T. Duerig, “Scaling up visual and vision-language representation learning with noisy text supervision,” in *International conference on machine learning*. PMLR, 2021, pp. 4904–4916.
- [20] Y. Ming, Z. Cai, J. Gu, Y. Sun, W. Li, and Y. Li, “Delving into out-of-distribution detection with vision-language representations,” *Advances in neural information processing systems*, vol. 35, pp. 35087–35102, 2022.
- [21] S. Esmaeilpour, B. Liu, E. Robertson, and L. Shu, “Zero-shot out-of-distribution detection based on the pre-trained model clip,” in *Proceedings of the AAAI conference on artificial intelligence*, vol. 36, no. 6, 2022, pp. 6568–6576.
- [22] J. Jeong, Y. Zou, T. Kim, D. Zhang, A. Ravichandran, and O. Dabeer, “Winclip: Zero-/few-shot anomaly classification and segmentation,” in *Proceedings of the IEEE/CVF Conference on Computer Vision and Pattern Recognition (CVPR)*, 2023, pp. 1994–2004.
- [23] P. Bergmann and D. Sattlegger, “Anomaly detection in 3d point clouds using deep geometric descriptors,” in *Proceedings of the IEEE/CVF Winter Conference on Applications of Computer Vision*, 2023, pp. 2613–2623.
- [24] Y. Bai, Z. Han, C. Zhang, B. Cao, X. Jiang, and Q. Hu, “Id-like prompt learning for few-shot out-of-distribution detection,” 2024. [Online]. Available: <https://arxiv.org/abs/2311.15243>
- [25] H. Sun, R. He, Z. Han, Z. Lin, Y. Gong, and Y. Yin, “Clip-os: Clip-driven outliers synthesis for few-shot ood detection,” *arXiv preprint arXiv:2404.00323*, 2024.
- [26] H. Wang, Y. Li, H. Yao, and X. Li, “Clipn for zero-shot ood detection: Teaching clip to say no,” in *Proceedings of the IEEE/CVF International Conference on Computer Vision (ICCV)*, 2023, pp. 2303–2313.
- [27] Y. Cong, S. Khanna, C. Meng, P. Liu, E. Rozi, Y. He, M. Burke, D. Lobell, and S. Ermon, “Satmae: Pre-training transformers for temporal and multi-spectral satellite imagery,” *Advances in Neural Information Processing Systems*, vol. 35, pp. 197–211, 2022.
- [28] K. Zhou, J. Yang, C. C. Loy, and Z. Liu, “Learning to prompt for vision-language models,” in *Proceedings of the IEEE/CVF Conference on Computer Vision and Pattern Recognition (CVPR)*, 2022, pp. 8765–8775.
- [29] J. Yang, K. Zhou, and Z. Liu, “Full-spectrum out-of-distribution detection,” *International Journal of Computer Vision*, vol. 131, no. 10, pp. 2607–2622, 2023.
- [30] Y. Ji, X. Xiao, G. Chen, H. Xu, C. Ma, L. Zhu, A. Liang, and J. Chen, “Cibr: Cross-modal information bottleneck regularization for robust clip generalization,” 2025. [Online]. Available: <https://arxiv.org/abs/2503.24182>
- [31] Z. Yang, W. Guan, L. Xiao, and H. Chen, “Few-shot object detection in remote sensing images via data clearing and stationary meta-learning,” *Sensors*, vol. 24, no. 12, p. 3882, 2024.
- [32] B. Xi, J. Li, Y. Li, R. Song, Y. Shi, S. Liu, and Q. Du, “Deep prototypical networks with hybrid residual attention for hyperspectral image classification,” *IEEE Journal of Selected Topics in Applied Earth Observations and Remote Sensing*, vol. 13, pp. 3683–3700, 2020.
- [33] B. Zhang, S. Feng, X. Li, Y. Ye, R. Ye, C. Luo, and H. Jiang, “Sgmmnet: Scene graph matching network for few-shot remote sensing scene classification,” *IEEE Transactions on Geoscience and Remote Sensing*, vol. 60, pp. 1–15, 2022.
- [34] Z. Li, M. Liu, Y. Chen, Y. Xu, W. Li, and Q. Du, “Deep cross-domain few-shot learning for hyperspectral image classification,” *IEEE Transactions on Geoscience and Remote Sensing*, vol. 60, pp. 1–18, 2022.
- [35] W. G. C. Bandara and V. M. Patel, “Revisiting consistency regularization for semi-supervised change detection in remote sensing images,” *arXiv preprint arXiv:2204.08454*, 2022.
- [36] B. Fang, Y. Li, H. Zhang, and J. C.-W. Chan, “Semi-supervised deep learning classification for hyperspectral image based on dual-strategy sample selection,” *Remote Sensing*, vol. 10, no. 4, p. 574, 2018.
- [37] Y. Yuan and L. Lin, “Self-supervised pretraining of transformers for satellite image time series classification,” *IEEE Journal of Selected Topics in Applied Earth Observations and Remote Sensing*, vol. 14, pp. 474–487, 2021.
- [38] O. Mañas, A. Lacoste, X. Giró-i Nieto, D. Vázquez, and P. Rodríguez, “Seasonal contrast: Unsupervised pre-training from uncurated remote sensing data,” in *Proceedings of the IEEE/CVF International Conference on Computer Vision*, 2021, pp. 9414–9423.
- [39] H. Al-Hichri, Y. Bazi, and M. M. Al-Rahhal, “Self-supervised learning for remote sensing scene classification under the few shot scenario,” *Scientific Reports*, vol. 12, no. 1, p. 3192, 2022.
- [40] Y. Liu, Y. Zhang, Z. Li, Y. Li, and J. He, “Srl-protonet: Self-supervised representation learning for few-shot remote sensing scene classification,” *IET Computer Vision*, vol. 18, no. 4, pp. 445–458, 2024.
- [41] J. Shenoy, X. D. Zhang, S. Mehrotra, B. Tao, R. Yang, H. Zhao, and D. Vasishth, “S4: Self-supervised sensing across the spectrum,” in

*Proceedings of the IEEE/CVF Conference on Computer Vision and Pattern Recognition Workshops*, 2024, arXiv:2405.01656.

- [42] D. Hendrycks and K. Gimpel, “A baseline for detecting misclassified and out-of-distribution examples in neural networks,” 2018. [Online]. Available: <https://arxiv.org/abs/1610.02136>
- [43] W. Liu, X. Wang, J. D. Owens, and Y. Li, “Energy-based out-of-distribution detection,” 2021. [Online]. Available: <https://arxiv.org/abs/2010.03759>
- [44] D. Hendrycks, S. Basart, M. Mazeika, A. Zou, J. Kwon, M. Mostajabi, J. Steinhardt, and D. Song, “Scaling out-of-distribution detection for real-world settings,” 2022. [Online]. Available: <https://arxiv.org/abs/1911.11132>
- [45] R. Chan, M. Rottmann, and H. Gottschalk, “Entropy maximization and meta classification for out-of-distribution detection in semantic segmentation,” 2021. [Online]. Available: <https://arxiv.org/abs/2012.06575>
- [46] S. Liang, Y. Li, and R. Srikant, “Enhancing the reliability of out-of-distribution image detection in neural networks,” in *International Conference on Learning Representations (ICLR)*, 2018.
- [47] Z. Chen, V. Badrinarayanan, C.-Y. Lee, and A. Rabinovich, “Gradnorm: Gradient normalization for adaptive loss balancing in deep multitask networks,” 2018. [Online]. Available: <https://arxiv.org/abs/1711.02257>